The Phosphate-Specific Transport System Gene *pstA1* Contributes to Rifampin Tolerance in *Mycobacterium tuberculosis*

Authors:

Carina Danchik[1, †], G. V. Anoushka Chinmayi[1, †], Gi Yong Lee[2], Joel S. Bader[3,4], Hyungjin Eoh[2,5], Petros C. Karakousis[1,6,7,*]

† These authors contributed equally to this work.

Authors' affiliations:

[1] Tuberculosis Research Advancement Center, Department of Medicine, Johns Hopkins School of Medicine, Baltimore, MD, USA

[2] Department of Immunology and Immune Therapeutics, Keck School of Medicine, University of Southern California, Los Angeles, CA, USA

[3] Institute for Computational Medicine, Johns Hopkins University, Baltimore, MD, USA

[4] Department of Biomedical Engineering, Johns Hopkins University, Baltimore, MD, USA

[5] Department of Ophthalmology, Keck School of Medicine, University of Southern California, Los Angeles, CA, USA

[6] Department of International Health, Johns Hopkins Bloomberg School of Public Health, Baltimore, MD, USA

[7] Department of Molecular Microbiology and Immunology, Johns Hopkins Bloomberg School of Public Health, Baltimore, MD, USA

* Corresponding Author: Petros C. Karakousis, Center for Tuberculosis Research, Division of Infectious Diseases, School of Medicine, 1550 Orleans Street, Room 110, Baltimore, MD 21287, (410) 502-8233 / FAX (410) 614-8173, Email: petros@jhmi.edu

Keywords: *Mycobacterium tuberculosis*, PstA1, rifampin, antibiotic tolerance, phosphate-specific transport

Abstract

Tuberculosis (TB) caused an estimated 10.8 million new cases and 1.25 million deaths in 2023. Antibiotic tolerance, the ability of bacteria to survive exposure to bactericidal antibiotics without genetic resistance mutations, contributes to the need for prolonged treatment. Targeting antibiotic tolerance mechanisms could promote accelerated clearance of *Mycobacterium tuberculosis* (*Mtb*), thereby improving medical adherence. Our previous forward genetic screen for rifampin tolerance genes identified *pstA1*, which is involved in phosphate-specific import. The ABC-type transporter permease PstA1 has previously been implicated in *Mtb* virulence, as mutants lacking this gene exhibit defective survival during phosphate limitation *in vitro*, in infected macrophages, and in immunocompetent mice. The minimum inhibitory concentration (MIC) of rifampin was not altered in a *pstA1* deletion mutant (Δ*pstA1*), suggesting this difference in susceptibility is not due to antibiotic resistance. Consistent with a role in rifampin tolerance, time-kill assays revealed a shift in the mean duration of killing (2-log reduction) from 1.6 days in wild-type to 1.0 day in Δ*pstA1*, and complementation partially restored this phenotype. We found that *pstA1* is specifically required for *Mtb* survival in the absence of exogenous inorganic phosphate and is important for adaptation to growth in culture without detergent, and within macrophages in an interferon-γ-dependent manner. Differential expression analysis revealed that Δ*pstA1* exhibited substantial transcriptional reprogramming with 58 differentially expressed genes, including altered expression of metabolic, DNA damage repair, and secretory pathways. PstA1 represents a novel drug target, and inhibitors could serve as adjunctive therapies to shorten treatment times, reducing opportunities for drug resistance emergence.

Importance

Tuberculosis remains one of the world's deadliest infectious diseases, causing over a million deaths annually. Current treatment requires months of antibiotic therapy, and poor adherence to these lengthy regimens contributes to the emergence of drug-resistant strains that are increasingly difficult to treat. A major barrier to shorter treatment is antibiotic tolerance, which allows bacteria to survive drug exposure without genetic resistance mutations. This study identifies the phosphate transport component PstA1 as a critical factor enabling *Mycobacterium tuberculosis* to tolerate the frontline antibiotic rifampin. Bacteria lacking *pstA1* are eliminated more rapidly by rifampin, demonstrating that this transporter actively promotes bacterial survival during treatment. These findings suggest that drugs targeting PstA1 could be combined with standard antibiotics to accelerate bacterial clearance, potentially shortening treatment duration and improving patient adherence. Such adjunctive therapies targeting tolerance mechanisms represent a promising strategy to combat tuberculosis and reduce the global burden of drug-resistant disease.

Introduction

Tuberculosis (TB) remains the leading cause of death from a single infectious agent, causing an estimated 10.8 million new cases and 1.25 million deaths in 2023 alone [1]. While effective regimens exist and three new drugs have been approved to treat TB since 2010, additional advances are needed to shorten treatment duration and improve treatment completion [2]. Current first-line TB treatment requires the use of multiple antibiotics for a minimum of six months to prevent relapse. A key reason for this lengthy treatment time is the presence of residual populations of bacteria that exhibit antibiotic tolerance– a phenotypic and reversible state in which bacteria become transiently insusceptible to antibiotics, requiring longer exposures to achieve bacterial eradication [3]. Bacteria can use a variety of adaptive mechanisms, collectively termed phenotypic tolerance, to adapt to and survive under stress conditions experienced within the host as well as antibiotic pressure [4]. The molecular mechanisms underlying antibiotic tolerance in *Mtb* are complex, involving transcriptional stress responses, metabolic adaptations, activation of drug efflux pumps, and changes in cell wall permeability [5]. Direct disruption

of *Mtb* antibiotic tolerance mechanisms is expected to result in more rapid bacillary killing, leading to shorter treatment times that may improve medical adherence and decrease opportunities for the development of antibiotic resistance [6].

We previously used transposon mutant sequencing (Tn-seq) to identify *Mtb* genes required for survival during exposure to bactericidal concentrations of the first-line drug rifampin. Among the top hits from this unbiased genome-wide approach were the phosphate-specific transport (Pst) genes *rv0820/phoT*, *rv0929/pstC2*, and *rv0930/pstA1* [7]. Notably, their homologs were also identified in our similar forward genetic screen in which *M. avium* was exposed to rifabutin, providing additional confidence in their significance and suggesting that Pst genes contribute to rifamycin tolerance across mycobacterial species [6]. Pst systems are comprised of four essential components: PstA and PstC are permeases that form a transmembrane channel complex; PstS is an extracellular protein that senses and captures phosphate from the environment; and PstB is an intracellular ATPase that provides energy for active transport of phosphate against its concentration gradient [8-10]. PstA1, which is co-expressed as part of the putative *Mtb* operon *pstS3-pstC2-pstA1* [11], is an important virulence factor required for *Mtb* survival during acidic stress [12] and phosphate depletion [13, 14], as well as for *Mtb* survival within macrophages [15] and for resistance to IFN-γ dependent immunity in mice [14]. PstA1 also plays important regulatory roles, as several substrates of the ESX-5 secretion system, as well as membrane vesicles, are hypersecreted in Δ*pstA1* mutants [16, 17]. Each of these phenotypes is mediated at least in part through the constitutive activation of RegX3, a response regulator of the PhoPR two-component system, in the absence of PstA1 [18, 19]. This regulatory connection links phosphate sensing to broader stress responses and virulence factor expression. Previous studies have shown that a *pstA1* deletion mutant was more susceptible to several drug combinations *in vitro* and to rifampin in a mouse model [20], providing initial evidence for a role in antibiotic tolerance. However, the molecular mechanisms underlying this phenotype have not been fully elucidated.

In this study, we have comprehensively characterized the role of *pstA1* in rifampin tolerance using phenotypic assays, transcriptomics, and metabolomics to explore the

114 underlying molecular mechanisms of its increased susceptibility. We have also studied
115 the role of PstA1 in *Mtb* growth and survival in phosphate-rich and phosphate-depleted
116 models of nutrient starvation and within macrophages, providing insights into how
117 phosphate transport contributes to bacterial adaptation under diverse stress conditions.
118 Our findings reveal new mechanistic insights into antibiotic tolerance and highlight the
119 potential for targeting phosphate transport pathways in TB treatment.

120 Results

121 Phosphate transport gene deletions confer rifampin hypersusceptibility

122 Our Tn-seq screen to identify *Mtb* genes required for tolerance to the sterilizing drug
123 rifampin identified three Pst genes, *rv0820/phoT*, *rv0929/pstC2*, and *rv0930/pstA1*,
124 among the top hits [7]. Their homologs were also found in a similar Tn-seq study of *M.*
125 *avium* exposed to rifabutin [6]. Notably, *pstC2* and *pstA1* are downstream components of
126 an *Mtb* operon including *pstS3* [22, 37]. To confirm that these three genes are co-
127 transcribed in the H37Rv strain under our experimental conditions, we performed RT-
128 PCR analysis using primers spanning the intergenic and intragenic regions of this operon.
129 Our results confirmed that *pstS3*, *pstC2*, and *pstA1* are co-expressed as a single
130 polycistronic mRNA transcript (Fig 1), validating the operonic structure for subsequent
131 studies.

132 Next, we generated individual targeted deletion strains for each of these three genes
133 using the ORBIT cloning system [21]. Cloning was validated via PCR of the 5' and 3' ends
134 of the insertion site, as well as with whole genome sequencing for Δ*pstA1* (SeqCenter,
135 Pittsburgh, PA) (Supplementary Figure S1). To validate our Tn-seq findings, we assessed
136 the activity of rifampin against each deletion strain using standard time-kill assays
137 following addition of 2.0 µg/ml rifampin. All three deletion strains showed increased
138 susceptibility to rifampin treatment compared to wildtype controls harboring empty
139 vectors. At day 6, Δ*phoT* showed a non-significant 0.9 $\log_{10}$ reduction in CFU compared
140 to control (adjusted P = 0.358; Fig. 2A). Δ*pstC2* demonstrated a more pronounced
141 phenotype with an additional 1.3 $\log_{10}$ reduction (adjusted P = 0.000189, Fig. 2B). Δ*pstA1*

142 exhibited the strongest susceptibility to rifampin, showing an additional 1.9 $\log_{10}$ reduction
143 in viable bacteria (adjusted P = 0.00742) relative to the isogenic wild-type control (Fig.
144 2C). The minimum duration of killing (MDK), defined as the time required to achieve a 2-
145 $\log_{10}$ reduction from the starting bacterial density, decreased by 0.4 days for Δ*phoT*, 1.1
146 days for Δ*pstC2*, and 0.6 days for Δ*pstA1* relative to controls. Consistent with a role for
147 each of these genes in *Mtb* tolerance, rather than resistance, to rifampin, each deletion
148 mutant showed minimal alterations in rifampin MIC values. The MIC values of rifampin
149 against Δ*phoT* and Δ*pstC2* were 0.03 µg/ml and that of Δ*pstA1* was 0.016 µg/ml (wild
150 type, 0.03-0.06 µg/ml).

151 **Complementation of *pstA1* partially restores wild-type rifampin tolerance**

152 Given the robust phenotype observed with Δ*pstA1*, and the possibility that deletion of
153 *pstC2* could have polar effects on *pstA1*, our subsequent studies focused on Δ*pstA1*. To
154 validate the *pstA1* deletion phenotype, we constructed a genetic complementation strain
155 (Δ*pstA1::pstA1*). Since *pstS3*, *pstC2*, and *pstA1* are co-transcribed as an operon, we
156 designed our complementation construct to include appropriate regulatory elements. The
157 *pstA1* coding sequence fused to the putative operonic promoter region (422 bp upstream
158 of *pstS3* plus the first 75 bp of *pstS3*) was cloned into the episomal mycobacterial vector
159 pMH94 and introduced into the Δ*pstA1* strain. Complementation was confirmed by PCR
160 of insert junctions and whole genome sequencing (Supplementary Figure S1). Time-kill
161 assays revealed that the minimum duration of killing (MDK) of rifampin for the
162 complement strain was 1.3 days, as compared to 1.6 days for the wild type and 1.0 day
163 for ΔpstA1 (Fig. 2D). MDK values differed significantly between all three strains (WT vs
164 ΔpstA1: p = 0.00004; WT vs pstA1 comp: p = 0.004; ΔpstA1 vs pstA1 comp: p = 0.0011,
165 one-way ANOVA with Tukey's multiple comparisons test). Thus, genetic complementation
166 of Δ*pstA1* partially restored wild-type rifampin tolerance.

167

168

169 **Δ*pstA1* exhibits phosphate-specific survival defects while maintaining rifampin**
170 **susceptibility under starvation conditions**

171 To characterize the broader physiological role of *pstA1*, we examined bacterial survival
172 under various stress conditions relevant to mycobacterial pathogenesis and persistence.
173 As multiple forms of nutrient starvation are known to induce a tolerance phenotype [13,
174 22, 23], we tested the ability of Δ*pstA1* to survive in both the PBS nutrient starvation model
175 used in our prior screen [7] and during inorganic phosphate limitation [13].

176 During nutrient starvation in phosphate-buffered saline containing the detergent tween-
177 80, both wild-type and Δ*pstA1* strains showed equivalent survival over a 14-day
178 adaptation period, with no significant differences observed between strains (Fig. 3A).
179 *ΔpstA1* retained enhanced rifampin susceptibility under nutrient-starved conditions.
180 When rifampin (2.0 µg/ml) was added after the 14-day starvation period, the deletion
181 mutant showed significantly enhanced killing compared to wild-type, with additional
182 reductions in viability becoming apparent by day 2 (1.4 $\log_{10}$ reduction; adjusted P =
183 0.000184) and persisting through day 6 (1.6 $\log_{10}$ reduction; adjusted P = 0.000184) (Fig.
184 3B).

185 Since phosphate depletion is known to induce the stringent response, a key antibiotic
186 tolerance pathway in *Mtb* [24, 25], and the *pstS3-pstC2-pstA1* operon and *phoT* are
187 upregulated under low phosphate conditions [13], we tested the ability of Δ*pstA1* to
188 survive in the absence of exogenous inorganic phosphate. Phosphate-specific depletion
189 revealed a clear survival disadvantage for Δ*pstA1*. While both wild-type and Δ*pstA1*
190 strains exhibited similar growth and survival characteristics in standard phosphate-rich
191 7H9 broth, Δ*pstA1* showed significantly reduced viability under phosphate-depleted
192 conditions. In modified 7H9 broth lacking inorganic phosphate, the deletion strain
193 demonstrated an additional survival defect with a 0.7 $\log_{10}$/ml decrease by day 7 (adjusted
194 P = 0.0115) and a 0.6 $\log_{10}$/ml decrease by day 14 (adjusted P = 0.00181) relative to wild
195 type (Fig. 3C). These results confirm the role of *pstA1* in phosphate acquisition under
196 limiting conditions and demonstrate its requirement for growth in low-phosphate
197 environments.

198 **Δ*pstA1* exhibits survival defects in IFN-γ-activated macrophages**

199 To assess the relevance of our findings to mycobacterial pathogenesis, we next examined
200 the role of *pstA1* in macrophage infection and intracellular survival as a model of the
201 natural host environment. Macrophages represent the primary host cell niche for *Mtb* and
202 create a hostile intracellular environment characterized by nutrient limitation, acidic pH,
203 and antimicrobial factor exposure [15]. We infected PMA-differentiated THP-1
204 macrophages with wild-type and Δ*pstA1* strains at a multiplicity of infection (MOI) of 1:1
205 and monitored intracellular bacterial survival over 4 days. In resting macrophages, there
206 was no significant difference in bacterial burden between wild-type and Δ*pstA1* at any
207 time point measured (days 0, 2, and 4 post-infection; Fig. 4A), suggesting that *pstA1* is
208 not required for initial invasion or survival in resting macrophages. However, when
209 macrophages were pre-activated with IFN-γ, a key cytokine that enhances macrophage
210 antimicrobial functions, Δ*pstA1* showed a significant survival defect that became
211 pronounced by day 4 post-infection. While wild-type bacteria maintained relatively high
212 intracellular numbers (4.2×10^6 CFU/ml), the Δ*pstA1* strain showed reduced survival
213 (2.43×10^6 CFU/ml), representing a statistically significant difference (adjusted $P = 0.0098$;
214 Fig. 4B). This result confirms previous reports that *pstA1* is specifically required for
215 resistance to IFN-γ-mediated host immunity and suggests a role in counteracting
216 activated macrophage antimicrobial mechanisms [15].

217 **The contribution of PstA1 to *Mtb* rifampin tolerance is not mediated through the**
218 **accumulation of inorganic polyphosphate**

219 Having established that Δ*pstA1* exhibits enhanced rifampin susceptibility, we next sought
220 to investigate the underlying mechanisms responsible for this phenotype. Induction of the
221 *Mtb* stringent response and accumulation of the multifunctional stress signaling molecule,
222 inorganic polyphosphate (polyP), has been linked to antibiotic tolerance in *Mtb* [26-30].
223 Since RegX3, a two-component response regulator that controls the *Mtb* phosphate
224 starvation and stringent responses [13, 31], is constitutively activated upon *pstA1* deletion
225 [14], we measured intracellular polyP levels as a proxy for stringent response activation.
226 No significant differences in polyP accumulation were observed between wild-type and

227 Δ*pstA1* strains across different growth phases (Fig. 5A). Wild-type polyP content ranged
228 from 3.072 to 5.536 ng/µg total protein, while Δ*pstA1* levels ranged from 3.673 to 5.915
229 ng/µg total protein.

230 **Δ*pstA1* exhibits increased rifampin uptake**

231 We hypothesized that *pstA1* deficiency might be associated with increased intrabacterial
232 accumulation of rifampin. Using a previously validated device that enables timed start-
233 stop measurements of antibiotics remaining in spent media [32], we quantified rifampin
234 content in the wild-type and mutant strains The kinetics of rifampin uptake revealed that
235 Δ*pstA1* displayed significantly faster and greater rifampin accumulation compared to wild-
236 type at 6 hours post-exposure, suggesting increased uptake and/or decreased efflux of
237 rifampin (Fig. 5B-C).

238 **Cell morphology analysis reveals minimal structural differences**

239 To determine whether the observed increase in rifampin uptake was attributable to gross
240 alterations in cell wall structure of the mutant, we examined bacterial morphology using
241 electron microscopy. Under standard growth conditions including Tween-80 to prevent
242 bacterial clumping, we observed no significant difference in cell length between the two
243 strains (average bacterial length= 2.34 µm for wild type and 2.26 µm for Δ*pstA1;* Fig. 5D).
244 Likewise, the strains showed similar average cell wall thicknesses of 21.18 nm and 19.61
245 nm, respectively (Fig. 5E). Substantial variations in cell wall thickness were observed for
246 both wild-type and Δ*pstA1* which appear similar to previously reported lipid inclusions
247 [33]. There were no significant differences in minimum, maximum, or average cell wall
248 thickness between the two strains.

249 Since use of detergent can alter cell wall permeability [34], the experiment was repeated
250 using cultures grown without Tween-80 (Fig. 5F-G). Cell length decreased for both strains
251 in detergent-free broth, from an average of 2.34 µm to 1.64 µm for wild-type and from
252 2.26 µm to 1.95 µm for Δ*pstA1* (difference= 0.31 µm; P = 0.0329; Fig. 5F). Cell wall
253 thickness did not vary notably between strains with averages of 15.37 nm for wild type
254 and 16.06 nm for Δ*pstA1*. The large variations in cell wall thickness seen in cultures grown

255 with Tween-80 were not present under detergent-free conditions (Fig. 5H). These results
256 demonstrate that Δ*pstA1* exhibits increased rifampin accumulation without major changes
257 in cellular morphology.

258 **Transcriptomic analysis reveals extensive metabolic and regulatory**
259 **reprogramming in Δ*pstA1***

260 To further explore the molecular mechanisms underlying the increased rifampin
261 susceptibility of Δ*pstA1* and identify potential cellular pathways contributing to enhanced
262 drug uptake, we performed transcriptomic analysis using RNA sequencing. Wild-type and
263 Δ*pstA1* strains were exposed to a sub-inhibitory concentration of rifampin (7.5 ng/ml,
264 representing 1/4 MIC) for 30 or 60 minutes. This concentration and timing were selected
265 to capture early transcriptional responses while minimizing the global transcriptional
266 inhibition that occurs at bactericidal concentrations of rifampin. During axenic growth in
267 nutrient-rich broth lacking rifampin, Δ*pstA1* exhibited substantial transcriptional
268 reprogramming compared to wild type, with 58 differentially expressed genes (DEGs)
269 identified: 49 upregulated and 9 downregulated (adjusted $P < 0.05$, $|\log_2$ fold change$| >$
270 1; Fig. 6A). Several genes known to be part of the phosphate regulon showed significant
271 upregulation, including *pstS3* ($\log_2$ fold change = 3.22), *pstC2* ($\log_2$ fold change = 2.50),
272 and the two-component regulatory system genes *senX3* ($\log_2$ fold change = 1.59) and
273 *regX3* ($\log_2$ fold change = 1.77), indicating constitutive activation of phosphate starvation
274 signaling.

275 KEGG pathway enrichment analysis revealed that genes involved in biosynthesis and
276 metabolic pathways were prominently represented among the DEGs (Fig. 6B). The
277 differentially expressed genes included fourteen PE/PPE family genes (9 upregulated, 5
278 downregulated), with upregulation of members of the ESX-5 locus and downregulation of
279 *pe31* ($\log_2$ fold change = -6.02) and *ppe60* ($\log_2$ fold change = -3.37). Genes encoding
280 four ESAT-6-like proteins were upregulated, namely *esxI* ($\log_2$ fold change = 3.65), *esxJ*
281 ($\log_2$ fold change = 2.59), esxV ($\log_2$ fold change = 3.14), and *esxW* ($\log_2$ fold change =
282 2.35). The redox-responsive transcriptional regulator *whiB3* ($\log_2$ fold change = 2.60), a
283 key regulator of thiol metabolism and oxidative stress responses, was also significantly

upregulated [12]. Additionally, eleven genes involved in DNA metabolism were upregulated in the mutant at baseline, including resolvases, transposases, and DNA helicases. Rifampin treatment led to a progressive reduction in the number of DEGs between strains. After 30 minutes of rifampin exposure, 41 genes remained differentially expressed between strains. After 60 minutes, 41 genes were differentially expressed, with 36 genes showing consistent differential expression across all three conditions (baseline, 30 min, and 60 min). A comprehensive Venn diagram analysis of DEG overlap across all treatment conditions is shown in Supplementary Figure S2. The DNA metabolism genes were no longer significantly differentially expressed following rifampin treatment, while the core set of 36 genes included the phosphate regulon genes, all four ESAT-6-like protein genes, twelve PE/PPE family genes, and *whiB3*.

RT-qPCR analysis of 11 selected genes confirmed the expression patterns observed in the RNA-seq dataset, with correlation coefficients exceeding 0.7 for all comparisons (Fig. 6D; Supplementary Figure S3). Validated genes included members of the phosphate starvation response (*pstC2*, $\log_2$ fold change = 2.50; *regX3*, $\log_2$ fold change = 1.77; *senX3*, $\log_2$ fold change = 1.59), metabolic enzymes (*udgA*, $\log_2$ fold change = 3.08; *mgtA*, $\log_2$ fold change = 3.04), the stress response regulator *whiB3* ($\log_2$ fold change = 2.60), and PE/PPE family protein genes (*ppe60*, $\log_2$ fold change = -3.37; *ppe65*, $\log_2$ fold change = 1.89). A complete list of all DEGs across all experimental conditions is provided in Supplementary Table S2.

Metabolomic analysis reveals altered antioxidant metabolites in Δ*pstA1*

To understand the biochemical consequences of increased rifampin accumulation in the deletion mutant, we performed targeted metabolomics analysis of rifampin-treated bacteria and analysis was focused on antioxidant pathways. We analyzed the intracellular abundance of 16 metabolites involved in antioxidant biosynthesis and redox homeostasis in the Δ*pstA1* mutant, wild-type, and complement strains at 6 hours post-rifampin exposure. The heatmap analysis of all measured antioxidant metabolites revealed distinct metabolic profiles between strains (Fig. 7A). While most metabolites, including L-glutamate, glycine, NADPH, glutathionylspermidine, and various glutathione derivatives,

313 showed trends toward increased abundance in Δ*pstA1*, these changes did not reach
314 statistical significance. The complement strain generally displayed metabolite levels
315 which were intermediate between wild-type and the deletion mutant, consistent with
316 partial restoration of the metabolic phenotype.

317 Following rifampin treatment, two antioxidant pathway metabolites showed trends toward
318 altered abundance in Δ*pstA1* compared to wild-type: ergothioneine and 5-oxoproline ($p <$
319 0.1, ANOVA; Fig. 7B). Ergothioneine, a sulfur-containing antioxidant, showed a trend
320 toward elevation in Δ*pstA1* compared to both wild-type and complement strains. This
321 trend is notable given that *whiB3*, which was upregulated 2.6-fold in the transcriptomic
322 analysis and confirmed by RT-qPCR, is a metabolic regulator involved in the production
323 of ergothioneine and mycothiol, which play an important role in detoxifying the oxidative
324 stress [35]. Similarly, 5-oxoproline, a glutamate derived metabolite, showed a trend
325 toward increased abundance in the deletion mutant [36]. The observed trends suggest
326 that Δ*pstA1* may exhibit hypersensitivity to rifampin largely because of alterations in
327 antioxidant metabolism following increased rifampin exposure.

328 **Discussion**

329 Components of the Pst system have been implicated in virulence, stress tolerance, and
330 antibiotic susceptibility in several bacterial pathogens, suggesting that phosphate-specific
331 transport pathways may represent promising targets for therapeutic intervention [14, 37].
332 This study establishes PstA1 as a critical determinant of rifampin tolerance in *Mtb* through
333 mechanisms distinct from drug resistance. Deletion of *pstA1* resulted in enhanced
334 rifampin killing without substantial change in MIC, a phenotype that remained consistent
335 across nutrient starvation conditions and correlated with reduced survival in IFN-γ-
336 activated macrophages. Integrative multi-omics analysis revealed that *pstA1* loss triggers
337 constitutive phosphate starvation signaling, leading to PE/PPE porin upregulation. These
338 findings raise the possibility that PE/PPE porin upregulation enhances membrane
339 permeability, thereby promoting rifampin uptake. Metabolic profiling revealed
340 nonsignificant upregulation of antioxidant pathways including ergothioneine and

341 glutathione biosynthesis, suggesting elevated oxidative stress resulting from increased
342 intracellular rifampin accumulation due to hyperpermeability [35].

343 In contrast to prior studies showing that *pstA1* deficiency reduces the MIC of rifampin by
344 8-fold, we found a more modest 2-fold decrease in the rifampin MIC against Δ*pstA1*. This
345 discrepancy may be due to differences in the parent strain used (Erdman vs. H37Rv) [20].
346 Notwithstanding these findings, we observed significantly increased rifampin activity
347 against Δ*pstA1* in time-kill assays, the standard approach for assessing antibiotic
348 tolerance [5].

349 Δ*pstA1* retained its rifampin hypersusceptibility under nutrient starvation and showed
350 reduced survival under phosphate depletion, consistent with previous reports [14, 15] and
351 validating its core metabolic function in phosphate acquisition. This metabolic vulnerability
352 extended to host-pathogen interactions. While a previous Tn-seq study found that *pstS3*,
353 *pstC2*, *pstA1*, and *phoT* were each important for macrophage survival under all activation
354 conditions tested [15], Δ*pstA1* showed a more nuanced phenotype in the current study,
355 with no survival defect in resting macrophages but significant reduction in intracellular
356 survival in IFN-γ-activated macrophages by day 4. This finding aligns well with that from
357 a separate study reporting that Δ*pstA1* retained full virulence in IFN-$\gamma^{-}/^{-}$ mice but showed
358 reduced chronic-phase survival in wild-type mice, establishing that PstA1 is specifically
359 required for surviving IFN-γ-mediated immunity [14].

360 To understand the mechanistic basis for enhanced rifampin susceptibility, we examined
361 drug uptake dynamics and cellular structure. We observed accelerated rifampin uptake
362 with significantly elevated drug accumulation by 6 hours, implicating increased drug
363 permeability and/or reduced efflux. Electron microscopy revealed no major structural
364 changes in cellular morphology. Our transcriptomic analysis provided insight into the
365 molecular basis for this altered permeability state. In the absence of rifampin exposure,
366 Δ*pstA1* showed extensive cellular reprogramming with 58 genes differentially expressed.
367 Most striking was the constitutive activation of the phosphate starvation regulon, including
368 *pstS3*, *pstC2*, *senX3*, and *regX3,* indicating that cells lacking functional PstA1 exist in a
369 state of perceived phosphate limitation regardless of environmental phosphate

370 availability. The marked upregulation of *pstS3* and *pstC2* likely represents compensatory
371 transcriptional upregulation consistent with constitutively activated RegX3, as multiple
372 studies have demonstrated RegX3-dependent regulation of the *pstS3-pstC2-pstA1*
373 operon [13, 14, 18]. Without the functional PstA1 permease, however, this transcriptional
374 response cannot restore phosphate transport, resulting in persistent phosphate starvation
375 signaling.

376 This baseline stress state likely compromises bacterial ability to respond effectively to
377 additional challenges like antibiotic exposure. There is substantial concordance between
378 our transcriptomic data and those of another study evaluating a *pstA1* deletion mutant in
379 the Erdman background, as 22 common DEGs were also identified in both studies,
380 including *senX3*, *regX3*, the *pstS3-pstC2-pstA1* operon, *whiB3*, and 9 PE/PPE genes,
381 validating the core transcriptional signature of *pstA1* deficiency across strain backgrounds
382 [14].

383 Among the 36 genes differentially expressed in *ΔpstA1* regardless of rifampin treatment,
384 12 encoded PE/PPE family genes and 4 encoded ESAT-6-like proteins. Four of these
385 PE/PPE genes (PE18, PPE19, PPE25, PPE27) are part of the *esx-5* locus, consistent
386 with established regulation of ESX-5 secretion by the Pst/SenX3-RegX3 axis and the
387 finding that *pstA1* deletion causes ESX-5 substrate hypersecretion. This upregulation
388 provides a direct mechanistic link to the increased rifampin uptake we observed [16].
389 Recent work demonstrated that Δ*pstA1* mutants overcome acid growth arrest by
390 upregulating PE19-PPE51 porin expression to enhance glycerol uptake [12], while
391 another study established that PE/PPE proteins function as substrate-specific outer
392 membrane channels [38]. The constitutive overexpression of multiple PE/PPE proteins in
393 Δ*pstA1* facilitates not only glycerol uptake but also rifampin entry through increased
394 membrane permeability, potentially explaining the accelerated drug accumulation and
395 enhanced killing [12]. Transcriptomic analysis revealed no downregulation of known
396 rifampin efflux pump genes, further supporting the hypothesis that enhanced drug
397 accumulation results from increased membrane permeability rather than impaired efflux.
398 The absence of gross structural defects on electron microscopy supports the

399 interpretation that increased permeability results from specific changes in channel
400 composition rather than general membrane disruption.

401 Interestingly, DNA-interacting genes were only upregulated in Δ*pstA1* in the absence of
402 rifampin, suggesting that drug's inhibitory effects on RNA polymerase may suppress
403 some baseline transcriptional differences. We identified only a few genes differentially
404 regulated exclusively upon rifampin exposure, likely because of the relatively low drug
405 concentration and brief timepoints, which were selected to minimize global transcriptional
406 inhibition.

407 Our integrated metabolomic and transcriptomic analysis revealed activation of antioxidant
408 pathways in rifampin-treated Δ*pstA1*, consistent with elevated oxidative stress from
409 increased intracellular drug accumulation. We observed an upward trend of metabolites
410 involved in antioxidant defense, including 5-oxoproline, glutamate,
411 glutathionylspermidine, and notably ergothioneine. The ergothioneine response is
412 particularly informative: this mycobacterial antioxidant provides protection against
413 rifampin-induced damage, as a study demonstrated that Δ*egtD* mutants lacking
414 ergothioneine show enhanced susceptibility to rifampin and other first-line drugs [39]. The
415 apparent paradox in Δ*pstA1*, where ergothioneine is elevated yet susceptibility increases,
416 could reflect compensatory antioxidant upregulation that is insufficient to overcome the
417 primary defect of PE/PPE-mediated drug hyperpermeability.

418 The concurrent 2.6-fold upregulation of *whiB3*, a redox-responsive regulator of thiol
419 metabolism, further supports activation of oxidative stress defenses. While one study
420 showed that WhiB3 negatively regulates ergothioneine biosynthesis under standard
421 conditions, the simultaneous increase in both *whiB3* expression and ergothioneine levels
422 in rifampin-treated Δ*pstA1* suggests that rifampin-induced oxidative stress may trigger
423 compensatory antioxidant production [35]. The elevation of 5-oxoproline, a glutamate-
424 derived metabolite, indicates broad activation of thiol-based defenses beyond
425 ergothioneine alone [40]. Critically, despite these activated protective pathways, Δ*pstA1*
426 exhibits marked hypersusceptibility to rifampin, suggesting that the primary driver of
427 enhanced killing is increased drug accumulation rather than deficient antioxidant capacity.

428 This is further supported by recent findings showing that WhiB3 expression is induced by
429 both acidic pH and phosphate limitation through RegX3-dependent mechanisms, and that
430 elevated WhiB3 levels in Δ*pstA1* correlate with reduced acid-induced ROS and preserved
431 GAPDH activity [12].

432 While increased rifampin uptake provides mechanistic connection to enhanced killing, the
433 molecular basis for altered drug accumulation requires further investigation. The link
434 between PE/PPE upregulation, ESX-5 hypersecretion, and rifampin permeability needs
435 direct demonstration. The transcriptomic analysis captures a snapshot of cellular
436 responses and may miss dynamic changes occurring at other timepoints. The targeted
437 metabolomics, while revealing specific antioxidant pathway alterations, can be extended
438 to look at relevant perturbations in central metabolism or lipid composition that could
439 contribute to the phenotype.

440 The identification of *pstA1* as a tolerance determinant opens potential therapeutic
441 avenues, and targeting this pathway requires careful consideration. Our findings show
442 that loss of PstA1 function creates multiple vulnerabilities, including enhanced drug
443 uptake, metabolic dysregulation, and impaired stress responses, suggesting that
444 constitutive activation of phosphate-sensing pathways during antibiotic treatment
445 becomes a liability rather than an adaptive advantage. The specific mechanisms identified
446 are intriguing targets: the WhiB3-ergothioneine stress response axis and PE/PPE-
447 mediated membrane changes represent downstream effectors that could be modulated
448 without disrupting fundamental phosphate homeostasis. Understanding how phosphate
449 transport influences antibiotic tolerance could inform adjunctive strategies to eliminate
450 persister populations, potentially shortening the lengthy treatment regimens currently
451 required for TB cure.

452

453

454

455 **Materials and Methods**

456 **Bacterial Strains and Plasmids**

457 *Mycobacterium tuberculosis* H37Rv served as the wild-type strain for all experiments.
458 Gene deletion strains were constructed using ORBIT (Oligonucleotide-Recombineering
459 followed by Bxb1 Integrase Targeting) cloning as previously described [94]. Wild-type
460 H37Rv was first transformed with pKM444, a non-integrating plasmid encoding RecT
461 recombinase and Bxb1 integrase (gift from Kenan Murphy, University of Massachusetts).
462 In a second electroporation, cells received pKM464 (also from Kenan Murphy) along with
463 a gene-specific oligonucleotide designed to delete pstA1. This oligonucleotide contained
464 the first and last 11 codons of pstA1 flanked by 37-bp homology arms, with the Bxb1 attP
465 integration site positioned centrally. Transformants were selected on antibiotic-selective
466 plates, and deletion junctions were verified by PCR amplification followed by Sanger
467 sequencing.

468 For complementation, the pstA1 coding sequence plus its upstream regulatory region
469 (422 bp upstream of pstS3 plus the first 75 bp of pstS3) was PCR-amplified from wild-
470 type H37Rv genomic DNA. This fragment was cloned into pMH94, an episomal
471 mycobacterial vector modified with apramycin resistance (gift from Dr. Gyanu
472 Lamichhane, Johns Hopkins University), using In-Fusion Snap Assembly (Takara Bio).
473 The vector was first linearized by restriction digestion with EcoRI and XbaI, gel-purified
474 using QIAquick Gel Extraction Kit (Qiagen), then assembled with the PCR product.
475 Cloned constructs were transformed into Stellar Competent Cells (Takara Bio), selected
476 on LB plates with appropriate antibiotics, and verified by PCR before electroporation into
477 the ΔpstA1 strain.

478 **Culture Conditions and Media**

479 *M. tuberculosis* strains were routinely cultured in Middlebrook 7H9 broth supplemented
480 with 10% OADC enrichment, 0.2% glycerol, and 0.05% Tween-80, or on Middlebrook
481 7H11 agar plates incubated at 37°C. Phosphate-depleted medium was prepared as
482 described previously [24] by omitting inorganic phosphate salts from the 7H9 formulation.

THP-1 monocytic cells were maintained in RPMI-1640 medium (Gibco) containing 2 mM L-glutamine and 10% heat-inactivated fetal bovine serum at 37°C with 5% CO_2.

Operon Structure Validation

To confirm co-expression of *pstS3*, *pstC2*, and *pstA1* as a single operon, RNA was extracted from logarithmically growing *Mtb* H37Rv cultures using TRIzol reagent. Following DNase-I treatment to eliminate genomic DNA contamination, RNA was reverse transcribed using SuperScript VILO cDNA Synthesis Kit (Invitrogen). PCR primers were designed to amplify both intragenic regions (within individual genes) and intergenic regions (spanning gene boundaries).

Whole Genome Sequencing Validation

High-molecular-weight genomic DNA was extracted from 10 mL log-phase cultures using an extended protocol optimized for mycobacteria. Cultures were lysed by sequential treatments with lysozyme (20 hours at 37°C), SDS/proteinase K (50°C), and CTAB, followed by chloroform/isoamyl alcohol extraction and isopropanol precipitation. To verify deletion and complementation, genomic DNA from wild type, Δ*pstA1*, and complement strains were submitted to SeqCenter (Pittsburgh, PA) for whole genome sequencing. Libraries were prepared using the Illumina DNA Prep kit with tagmentation-based fragmentation and sequenced on an Illumina NovaSeq X Plus platform (2×151 bp paired-end reads). Raw sequencing reads were aligned to the *M. tuberculosis* H37Rv reference genome, and coverage analysis was performed using SAMtools v1.18. Deletion boundaries were confirmed by examining read coverage across the *pstA1* locus.

Drug Susceptibility Testing

Minimum inhibitory concentrations (MICs) were determined by broth microdilution in 96-well plates. Bacterial suspensions were prepared by washing log-phase cultures and resuspending in Tween-80-free 7H9 medium to OD_{600} 0.01. Equal volumes (100 µL) of bacterial suspension and 2× serial drug dilutions were combined and incubated at 37°C for 6 days. Metabolic activity was assessed by adding 50 µL alamarBlue reagent (1:1

510 mixture of 10× alamarBlue and 10% Tween-80) and measuring fluorescence after 24
511 hours (544/590 nm excitation/emission) on a Fluostar OPTIMA plate reader (BMG
512 Labtech).

513 **Transmission Electron Microscopy**

514 Transmission electron microscopy was performed previously [27]. Briefly, mid-log phase
515 bacteria were collected and resuspended in 3% formaldehyde, 2.0% glutaraldehyde, 80
516 mM Sorenson's phosphate, and 4 mM MgCl2, pH 7.2 with duplicate samples for negative
517 staining and sectioning. Samples were fixed overnight at 4°C before processing and
518 imaging. Cell wall thickness was measured at two locations per bacterium: one in a thin
519 region and one in a thick region when present, to account for regional variations.

520 **Time-Kill Assays**

521 For nutrient-rich conditions, bacterial cultures were grown to mid-logarithmic phase in
522 complete 7H9 medium, then diluted to OD_{600} 0.05 one day prior to drug exposure. On
523 day 0, rifampin was added to a final concentration of 2 µg/mL unless otherwise noted
524 (stock: 2 mg/mL in DMSO), with vehicle controls receiving equivalent DMSO volumes.
525 Each condition was performed in triplicate using 5 mL cultures in 50 mL conical tubes,
526 incubated at 37°C with shaking. Bacterial viability was quantified by serial dilution plating
527 on 7H11 agar at days 2, 4, and 6 post-treatment. Plates were incubated at 37°C for 14-
528 21 days before colony counting.

529 For nutrient starvation conditions, log-phase cultures were washed and resuspended in
530 PBS containing 0.05% Tween-80 to OD_{600} 0.5, then incubated without shaking at 37°C
531 for 14 days to establish nutrient-deprivation. Rifampin (2 µg/mL) or vehicle control was
532 then added, and bacterial survival was monitored by CFU plating as described above.

533 For phosphate depletion experiments, cultures were washed twice and resuspended in
534 phosphate-free 7H9 medium to OD_{600} 0.05. Growth and survival were monitored over
535 time by CFU enumeration, with samples taken at indicated intervals during incubation at
536 37°C with shaking.

537 **Macrophage Infection Assays**

538 THP-1 cells were differentiated by treatment with 50 ng/mL phorbol 12-myristate 13-
539 acetate (PMA) for 48 hours at 37°C with 5% CO_2. Differentiated macrophages were
540 optionally activated with 20 ng/mL recombinant IFN-γ for 24 hours before infection.
541 Bacterial suspensions were prepared from log-phase cultures and used to infect
542 macrophages at a multiplicity of infection (MOI) of 1:1. After 4 hours, extracellular bacteria
543 were removed by washing three times with PBS, and fresh medium was added. At
544 specified time points, macrophages were lysed with 0.05% SDS and lysates were plated
545 on 7H11 agar for CFU determination.

546 **Polyphosphate Quantification**

547 Polyphosphate levels were measured as described previously [41]. Bacterial pellets were
548 lysed in guanidine thiocyanate buffer (5 M guanidine thiocyanate, 50 mM Tris-HCl pH 7.0)
549 using bead beating (3 cycles, 20 seconds at 6,800 rpm). After centrifugation, supernatants
550 were stored at -20°C, and protein concentrations were determined using DC Protein
551 Assay (Bio-Rad) for normalization. Polyphosphate was isolated using the GeneClean III
552 Kit (MP Biomedicals) following manufacturer protocols, including RNase/DNase
553 treatment to remove nucleic acids. Polyphosphate concentrations were determined
554 fluorometrically using DAPI staining (100 µg/mL final concentration) with
555 excitation/emission at 415/525 nm.

556 **Transcriptomic Analysis**

557 Wild-type and Δ*pstA1* cultures were grown to mid-log phase (OD_{600} ~0.5) in 45 mL 7H9
558 medium. To capture early transcriptional responses, cultures were treated with
559 subinhibitory rifampin (7.5 ng/mL, 1/4 MIC) or vehicle. RNA samples were collected at
560 baseline, 30- or 60-minutes post-treatment with three independent biological replicates
561 per condition.

562 Bacterial pellets (15 mL culture) were resuspended in TRIzol with 0.1 mm zirconia beads
563 and lysed using a Precellys Evolution homogenizer (3 cycles, 30 seconds at 7,400 rpm).

564 RNA was extracted with chloroform, precipitated with ethanol, and purified on RNeasy
565 columns (Qiagen) with on-column DNase I digestion. Following polyA selection, strand-
566 specific libraries were prepared using NEBNext Ultra II Directional RNA Library Prep Kit
567 and sequenced on Illumina NovaSeq X Plus (2×150 bp paired-end) at the Johns Hopkins
568 Genetic Resources Core Facility.

569 Raw reads were quality-assessed (FastQC v0.12.1) [30] and aligned to the *M.*
570 *tuberculosis* H37Rv reference genome (Bowtie2 v2.5.1) [31]. Gene counts were
571 quantified with featureCounts (Subread v2.0.0) [32]. Differential expression analysis used
572 DESeq2 v1.44.0 with significance thresholds of adjusted p-value < 0.05 (Benjamini-
573 Hochberg) and $|\log_2 FC| > 1$. Pathway analysis was performed using KEGGREST to query
574 KEGG pathways [34] for significantly differentially expressed genes.

575 **RT-qPCR Validation**

576 Twelve genes were analyzed by RT-qPCR, including eleven target genes and sigA as a
577 housekeeping control (18-22 nt, 100-147 bp amplicons) designed with IDT PrimerQuest
578 (Supplementary Table S1). Total RNA (500 ng) was DNase-treated, purified on RNeasy
579 columns, and reverse transcribed with iScript RT Master Mix (Bio-Rad) alongside no-RT
580 controls. qPCR used 10 µL reactions with SYBR Green Supermix on a QuantStudio 3
581 system (95°C/10 min; 40 cycles: 95°C/15s, 60°C/1 min). Relative expression was
582 calculated using the ΔΔCt method with sigA normalization.

583 **Metabolite extraction and LC-MS analysis**

584 *Mtb*-laden filters were incubated on m7H10 plates at 37°C for 5 days to mid-log phase
585 [35]. Cells were quenched with prechilled acetonitrile:methanol:H_2O (40:40:20, v:v:v) at
586 −40°C. Metabolites were extracted through mechanical lysis using 0.1-mm zirconia beads
587 in a Precellys tissue homogenizer for 2 min at 6,000 rpm, repeated three times under
588 continuous cooling at ≤2°C. Cell lysates were clarified by filtration through 0.22-µm Spin-
589 X columns. Residual protein content was measured with a BCA protein assay kit (Thermo
590 Scientific) to normalize metabolite ion counts to cell biomass.

591 Extracted metabolites were separated using a Cogent Diamond Hydride Type C column
592 with mobile phases of solvent A (ddH_2O with 0.2% formic acid) and solvent B (acetonitrile
593 with 0.2% formic acid). An Agilent 6230 TOF mass spectrometer was coupled to an
594 Agilent 1290 LC system. Dynamic mass axis calibration was maintained via continuous
595 infusion of reference mass solution through an isocratic pump with a 100:1 splitter. This
596 setup achieved mass errors of ~5 ppm and mass resolution of 10,000-25,000 over m/z
597 range 62–966, with a dynamic range of 5 $\log_{10}$. Ions were identified based on unique
598 accurate mass and retention time. Data analysis used Agilent Profinder B.07.00 with
599 mass tolerance <0.005 Da. All metabolomics data represent the average of at least two
600 independent triplicates.

601 **Antibiotic permeability (rifampin uptake)**

602 Rifampin uptake was measured using a previously validated device that enables timed
603 start-stop measurements of antibiotics in spent media [35, 36]. The device comprises a
604 plastic inset containing m7H9 with known antibiotic concentration. *Mtb*-laden filters were
605 generated using wild-type, ΔpstA1, and complement strains and placed onto media
606 containing 1 µg/mL rifampin at 37°C. After incubating for 2, 6, and 24 hours, bacterial
607 lysates and spent m7H9 were analyzed for rifampin content by LC-MS. Rifampin uptake
608 was calculated as: [RIF]drug only – [RIF]filtrate, with three biological replicates.

609 **Statistical Analysis**

610 Data are presented as mean ± standard deviation unless otherwise noted. Statistical
611 comparisons were performed using appropriate tests as specified in figure legends
612 (unpaired t-tests, one-way or two-way ANOVA with post-hoc corrections). Multiple
613 comparisons were corrected using the Holm-Sidak method or Tukey's Multiple
614 Comparisons where applicable. Statistical significance was defined as $p < 0.05$. Sample
615 sizes are indicated in individual figure legends.

616

617

Code and Data Availability

Code to replicate the performed analysis is available at https://doi.org/10.5281/zenodo.17344250. Raw sequencing data has been deposited to the Gene Expression Omnibus (GEO) and can be accessed at GSE310692. Additional data supporting the findings of this study are available upon request.

Acknowledgements:

We thank Dr. Kenan Murphy (University of Massachusetts) for generously providing the pKM444 and pKM464 plasmids used for ORBIT cloning, and Dr. Gyanu Lamichhane (Johns Hopkins University) for providing the pMH94 episomal vector. We are grateful to Megan Gelement (Johns Hopkins University) for contributions to methodology and data analysis discussions. We are grateful to SeqCenter (Pittsburgh, PA) for whole genome sequencing services. We thank the Johns Hopkins Genetic Resources Core Facility (GRCF) for RNA sequencing services.

Funding:

These studies were supported by NIAID/NIH grants R21 AI167027 to PCK ; R01AI168088 to HE. The funding source had no role in the study design, data collection, data analysis, data interpretation or writing of the report. The content is solely the responsibility of the authors and does not necessarily represent the official views of the National Institutes of Health.

Author Contributions:

Conceptualization: CD, PCK; Methodology: CD, GVAC, JSB, GYL, HE, PCK; Data acquisition: CD, GVAC, GYL; Data analysis: CD, GVAC, GYL; Supervision: JSB, HE, PCK; Funding acquisition: PCK, HE; Writing of original draft: CD, GVAC, PCK; Writing—review & editing: CD, GVAC, JSB, GYL, HE, PCK

643 **Competing Interests:**

644 All authors declare that they have no competing interests.

645 **References:**

646 1. *Global tuberculosis report*. 2023, World Health Organization: Geneva.
647 2. Nuermberger, E.L. and R.E. Chaisson, *Restocking the tuberculosis drug arsenal.*
648 Nature medicine, 2024. **30**(3): p. 642–643.
649 3. Balaban, N.Q., et al., *Definitions and guidelines for research on antibiotic*
650 *persistence.* Nature Reviews Microbiology, 2019. **17**(7): p. 441–448.
651 4. Joshi, H., D. Kandari, and R. Bhatnagar, *Insights into the molecular determinants*
652 *involved in Mycobacterium tuberculosis persistence and their therapeutic*
653 *implications.* Virulence, 2021. **12**(1): p. 2721–2749.
654 5. Brauner, A., et al., *Distinguishing between resistance, tolerance and persistence*
655 *to antibiotic treatment.* Nature Reviews Microbiology, 2016. **14**(5): p. 320–330.
656 6. Matern, W.M., et al., *Genetic Determinants of Intrinsic Antibiotic Tolerance in*
657 *Mycobacterium avium.* Microbiology Spectrum, 2021. **9**(2).
658 7. Matern, W.M., et al., *Functional Whole Genome Screen of Nutrient-Starved*
659 *Mycobacterium tuberculosis Identifies Genes Involved in Rifampin Tolerance.*
660 Microorganisms, 2023. **11**(9): p. 2269–2269.
661 8. Braibant, M., et al., *Identification of a second Mycobacterium tuberculosis gene*
662 *cluster encoding proteins of an ABC phosphate transporter.* FEBS Letters, 1996.
663 **394**(2): p. 206–212.
664 9. Pelly, S., et al., *REMap: Operon map of M. tuberculosis based on RNA sequence*
665 *data.* Tuberculosis, 2016. **99**: p. 70–80.
666 10. Tischler, A.D., et al., *Mycobacterium tuberculosis Phosphate Uptake System*
667 *Component PstA2 Is Not Required for Gene Regulation or Virulence.* PLOS ONE,
668 2016. **11**(8): p. e0161467–e0161467.
669 11. Vanzembergh, F., et al., *Effect of PstS sub-units or PknD deficiency on the survival*
670 *of Mycobacterium tuberculosis.* Tuberculosis (Edinburgh, Scotland), 2010. **90**(6):
671 p. 338–45.

672 12. Healy, C., S. Ehrt, and A. Gouzy, *An exacerbated phosphate starvation response*
673 *triggers Mycobacterium tuberculosis glycerol utilization at acidic pH.* mBio, 2025.
674 **16**(1).
675 13. Rifat, D., William R. Bishai, and Petros C. Karakousis, *Phosphate Depletion: A*
676 *Novel Trigger for Mycobacterium tuberculosis Persistence.* The Journal of
677 Infectious Diseases, 2009. **200**(7): p. 1126–1135.
678 14. Tischler, A.D., et al., *Mycobacterium tuberculosis Requires Phosphate-Responsive*
679 *Gene Regulation To Resist Host Immunity.* Infection and Immunity, 2013. **81**(1): p.
680 317–328.
681 15. Rengarajan, J., B.R. Bloom, and E.J. Rubin, *Genome-wide requirements for*
682 *Mycobacterium tuberculosis adaptation and survival in macrophages.* Proceedings
683 of the National Academy of Sciences, 2005. **102**(23): p. 8327–8332.
684 16. Elliott, S.R. and A.D. Tischler, *Phosphate responsive regulation provides insights*
685 *for ESX-5 function in Mycobacterium tuberculosis.* Current Genetics, 2016. **62**(4):
686 p. 759–763.
687 17. White, D.W., et al., *Mycobacterium tuberculosis Pst/SenX3-RegX3 Regulates*
688 *Membrane Vesicle Production Independently of ESX-5 Activity.* mBio, 2018. **9**(3).
689 18. Rifat, D., D.A. Belchis, and P.C. Karakousis, *senX3-independent contribution of*
690 *regX3 to Mycobacterium tuberculosis virulence.* BMC microbiology, 2014. **14**: p.
691 265–265.
692 19. Rifat, D. and P.C. Karakousis, *Differential regulation of the two-component*
693 *regulatory system senX3-regX3 in Mycobacterium tuberculosis.* Microbiology
694 (Reading, England), 2014. **160**(Pt 6): p. 1125–1133.
695 20. Namugenyi, S.B., et al., *Mycobacterium tuberculosis PhoY Proteins Promote*
696 *Persister Formation by Mediating Pst/SenX3-RegX3 Phosphate Sensing.* mBio,
697 2017. **8**(4).
698 21. Murphy, K.C., et al., *ORBIT: a New Paradigm for Genetic Engineering of*
699 *Mycobacterial Chromosomes.* mBio, 2018. **9**(6).
700 22. Betts, J.C., et al., *Evaluation of a nutrient starvation model of Mycobacterium*
701 *tuberculosis persistence by gene and protein expression profiling.* Molecular
702 Microbiology, 2002. **43**(3): p. 717–731.

703 23. Xie, Z., N. Siddiqi, and E.J. Rubin, *Differential Antibiotic Susceptibilities of Starved*
704 *Mycobacterium tuberculosis Isolates.* Antimicrobial Agents and Chemotherapy,
705 2005. **49**(11): p. 4778–4780.
706 24. Danchik, C., S. Wang, and P.C. Karakousis, *Targeting the Mycobacterium*
707 *tuberculosis Stringent Response as a Strategy for Shortening Tuberculosis*
708 *Treatment.* Frontiers in microbiology, 2021. **12**: p. 744167–744167.
709 25. Dutta, N.K., et al., *Inhibiting the stringent response blocks Mycobacterium*
710 *tuberculosis entry into quiescence and reduces persistence.* Science Advances,
711 2019. **5**(3).
712 26. Thayil, S.M., et al., *The role of the novel exopolyphosphatase MT0516 in*
713 *Mycobacterium tuberculosis drug tolerance and persistence.* PloS one, 2011.
714 **6**(11): p. e28076–e28076.
715 27. Chuang, Y.-M., et al., *Deficiency of the Novel Exopolyphosphatase Rv1026/PPX2*
716 *Leads to Metabolic Downshift and Altered Cell Wall Permeability in Mycobacterium*
717 *tuberculosis.* mBio, 2015. **6**(2).
718 28. Chuang, Y.-M., et al., *Stringent Response Factors PPX1 and PPK2 Play an*
719 *Important Role in Mycobacterium tuberculosis Metabolism, Biofilm Formation, and*
720 *Sensitivity to Isoniazid In Vivo.* Antimicrobial agents and chemotherapy, 2016.
721 **60**(11): p. 6460–6470.
722 29. Chugh, S., et al., *Polyphosphate kinase-1 regulates bacterial and host metabolic*
723 *pathways involved in pathogenesis of Mycobacterium tuberculosis.* Proceedings
724 of the National Academy of Sciences of the United States of America, 2024. **121**(2):
725 p. e2309664121–e2309664121.
726 30. Singh, R., et al., *Polyphosphate deficiency in Mycobacterium tuberculosis is*
727 *associated with enhanced drug susceptibility and impaired growth in guinea pigs.*
728 Journal of bacteriology, 2013. **195**(12): p. 2839–51.
729 31. Sureka, K., et al., *Polyphosphate kinase is involved in stress-induced mprAB-sigE-*
730 *rel signalling in mycobacteria.* Molecular microbiology, 2007. **65**(2): p. 261–76.
731 32. Eoh, H. and K.Y. Rhee, *Multifunctional essentiality of succinate metabolism in*
732 *adaptation to hypoxia in Mycobacterium tuberculosis.* Proceedings of the National
733 Academy of Sciences, 2013. **110**(16): p. 6554–6559.

734 33. Vijay, S., et al., *Ultrastructural Analysis of Cell Envelope and Accumulation of Lipid*
735 *Inclusions in Clinical Mycobacterium tuberculosis Isolates from Sputum, Oxidative*
736 *Stress, and Iron Deficiency.* Frontiers in Microbiology, 2018. **8**.
737 34. Leisching, G., et al., *Virulence, biochemistry, morphology and host-interacting*
738 *properties of detergent-free cultured mycobacteria: An update.* Tuberculosis, 2016.
739 **100**: p. 53–60.
740 35. Saini, V., et al., *Ergothioneine Maintains Redox and Bioenergetic Homeostasis*
741 *Essential for Drug Susceptibility and Virulence of Mycobacterium tuberculosis.* Cell
742 Reports, 2016. **14**(3): p. 572–585.
743 36. Rieck, B., et al., *PknG senses amino acid availability to control metabolism and*
744 *virulence of Mycobacterium tuberculosis.* PLoS pathogens, 2017. **13**(5): p.
745 e1006399–e1006399.
746 37. Lamarche, M.G., et al., *The phosphate regulon and bacterial virulence: a*
747 *regulatory network connecting phosphate homeostasis and pathogenesis.* FEMS
748 microbiology reviews, 2008. **32**(3): p. 461–73.
749 38. Wang, Q., et al., *PE/PPE proteins mediate nutrient transport across the outer*
750 *membrane of Mycobacterium tuberculosis.* Science (New York, N.Y.), 2020.
751 **367**(6482): p. 1147–1151.
752 39. Richard-Greenblatt, M., et al., *Regulation of Ergothioneine Biosynthesis and Its*
753 *Effect on Mycobacterium tuberculosis Growth and Infectivity.* The Journal of
754 biological chemistry, 2015. **290**(38): p. 23064–76.
755 40. Trivedi, A., et al., *Thiol reductive stress induces cellulose-anchored biofilm*
756 *formation in Mycobacterium tuberculosis.* Nature Communications, 2016. **7**(1): p.
757 11392–11392.
758 41. Chuang, Y.-M., D.A. Belchis, and P.C. Karakousis, *The Polyphosphate Kinase*
759 *Gene ppk2 Is Required for Mycobacterium tuberculosis Inorganic Polyphosphate*
760 *Regulation and Virulence.* mBio, 2013. **4**(3).

761

762

763

764 **Figures**

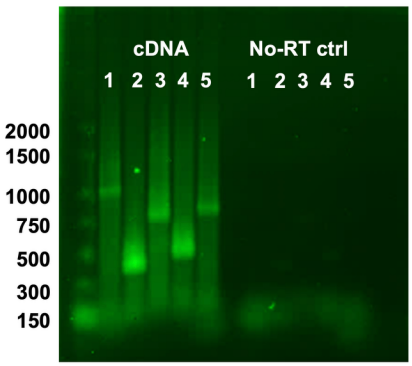

Lane	Region Amplified	Band Size
1	pstS3	1028 bp
2	pstS3-pstC2 junction	414 bp
3	pstC2	755 bp
4	pstC2-pstA1 junction	483 bp
5	pstA1	810 bp

765

766 **Figure 1. The *pstS3-pstC2-pstA1* genes are co-transcribed as an operon.** RT-PCR
767 analysis of H37Rv total RNA using primers spanning intragenic regions within *pstS3* (lane
768 1), *pstC2* (lane 3), and *pstA1* (lane 5), or intergenic junctions between *pstS3-pstC2* (lane
769 2) and *pstC2-pstA1* (lane 4). Amplification of all regions from cDNA confirms continuous
770 transcription across the three genes. No-RT controls (right panel) show the absence of
771 genomic DNA contamination. Expected amplicon sizes are indicated in the table.

772

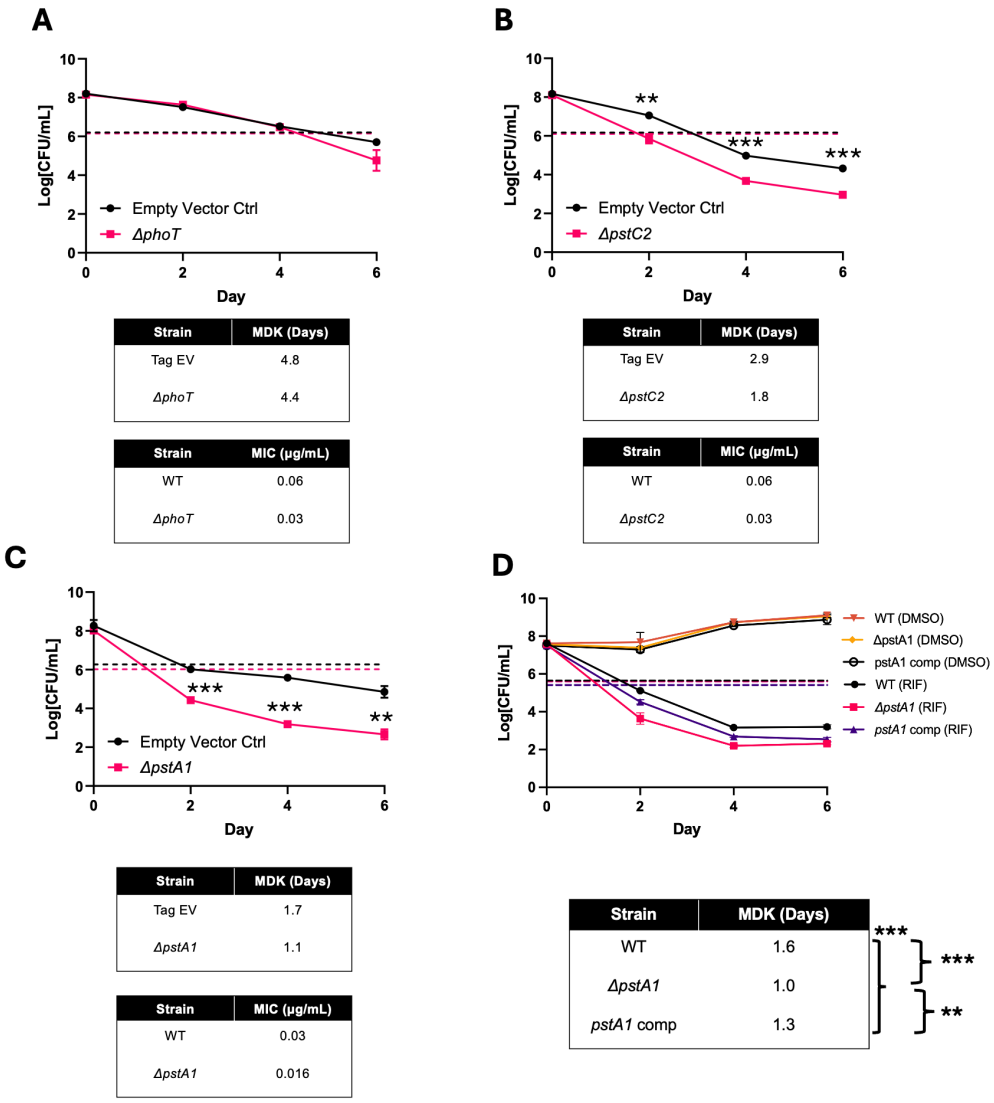

Strain	MDK (Days)
Tag EV	4.8
ΔphoT	4.4

Strain	MIC (µg/mL)
WT	0.06
ΔphoT	0.03

Strain	MDK (Days)
Tag EV	2.9
ΔpstC2	1.8

Strain	MIC (µg/mL)
WT	0.06
ΔpstC2	0.03

Strain	MDK (Days)
Tag EV	1.7
ΔpstA1	1.1

Strain	MIC (µg/mL)
WT	0.03
ΔpstA1	0.016

Strain	MDK (Days)
WT	1.6
ΔpstA1	1.0
pstA1 comp	1.3

773

774 **Figure 2. Deletion of phosphate-specific transport genes enhances rifampin**
775 **susceptibility.** Time-kill assays were performed in 7H9 medium with 2 µg/mL rifampin for
776 (A) ΔphoT, (B) ΔpstC2, and (C) ΔpstA1 in parallel with an empty vector control. (D) Time-
777 kill assays performed with 7H9 medium with 0.5 µg/mL rifampin on wild-type, ΔpstA1 and
778 pstA1 complement strains. Dotted lines indicate 2-$\log_{10}$ reduction from starting inoculum.
779 Tables show minimum duration of killing (MDK) to achieve 2-$\log_{10}$ reduction and rifampin
780 MIC values for each strain. Statistical significance for CFU comparisons at individual
781 timepoints (A-C) was determined by unpaired t-test with Holm-Šídák correction for
782 multiple comparisons. Statistical significance for MDK values (D) was determined by one-
783 way ANOVA with Tukey's multiple comparisons test (*P ≤ 0.05; **P ≤ 0.01; ***P ≤ 0.001).

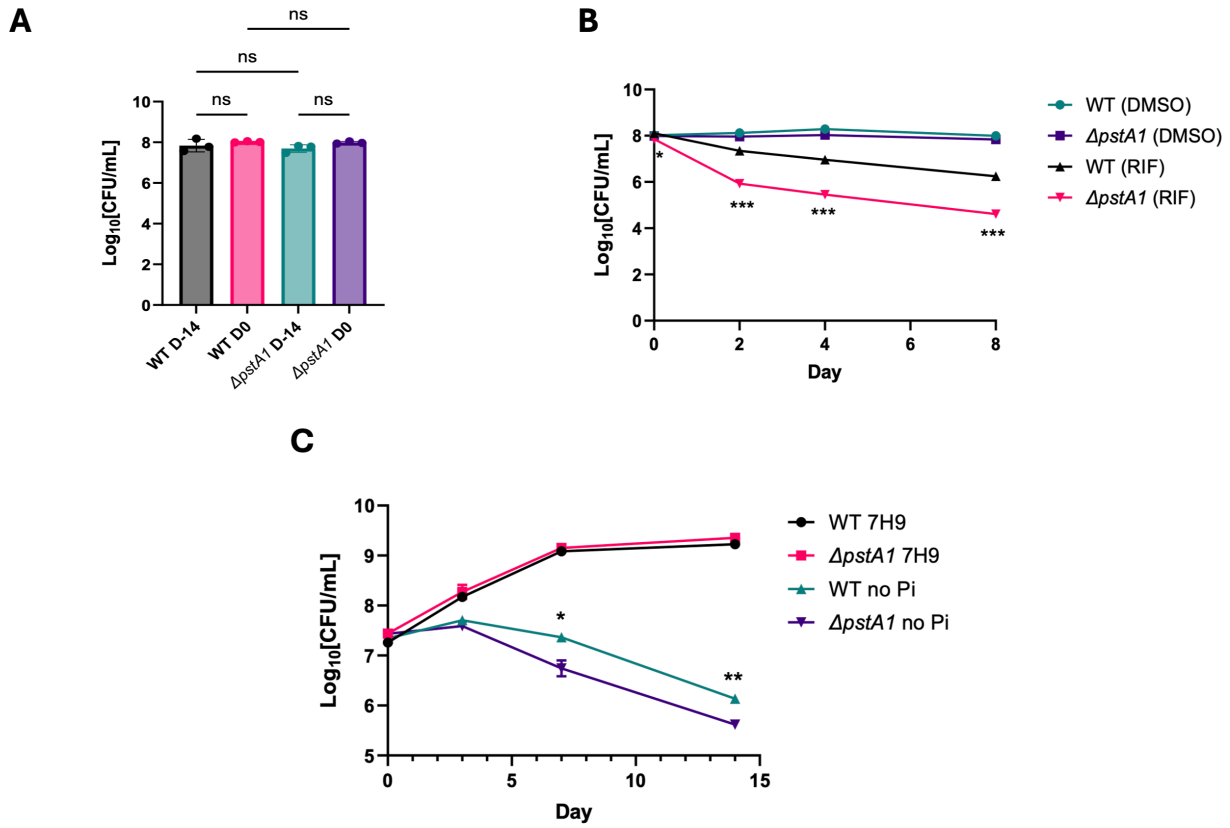

Figure 3. Δ*pstA1* survival under nutrient starvation and phosphate depletion. (**A**) Wild-type H37Rv and Δ*pstA1* survival after exposure to PBS-Tween for 14 days. No significant differences were observed by one-way ANOVA followed by Tukey's multiple comparisons test. (**B**) Δ*pstA1* maintained increased rifampin sensitivity after 2 weeks of PBS pre-treatment. Bacteria were treated with 2 µg/mL rifampin or DMSO vehicle control. Statistical differences indicated are for WT (RIF) vs Δ*pstA1* (RIF). Representative of two independent experiments.

(**C**) Δ*pstA1* shows no growth defect in phosphate-rich 7H9 medium but exhibits accelerated death under phosphate depletion (no Pi). Statistical differences shown are between WT no Pi and Δ*pstA1* no Pi conditions. Representative of three independent experiments.

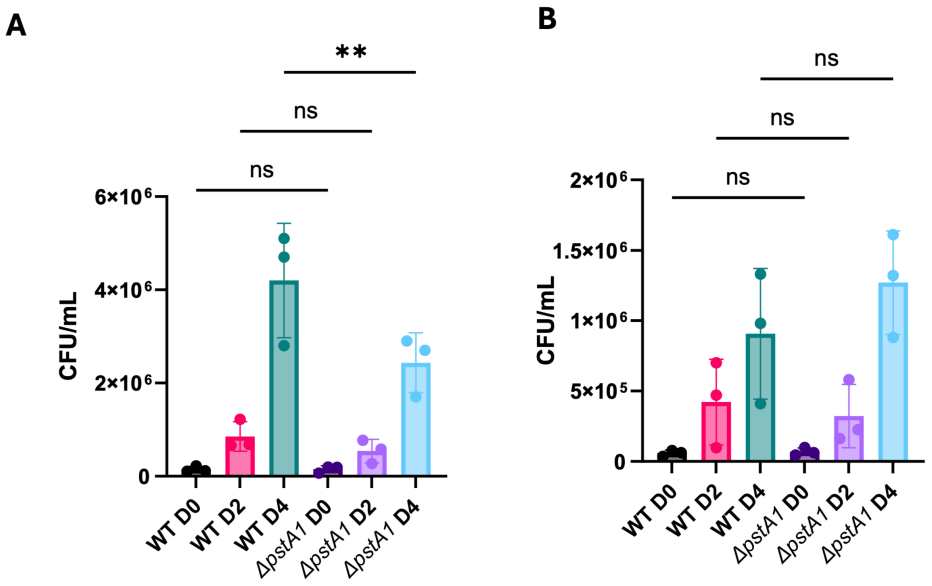

Figure 4. Δ*pstA1* exhibits an IFN-γ-dependent growth defect within macrophages. Bacterial burden within PMA-differentiated THP1 cells after 4 hours of infection (D0) or 2 or 4 days without (A) or with (B) 24 hr IFN-γ polarization before infection. One way ANOVA was performed followed by Sidak's multiple comparisons test to determine significance. Adjusted p- value ≤0.05 = *; ≤0.01 = **; ≤0.001 = ***.

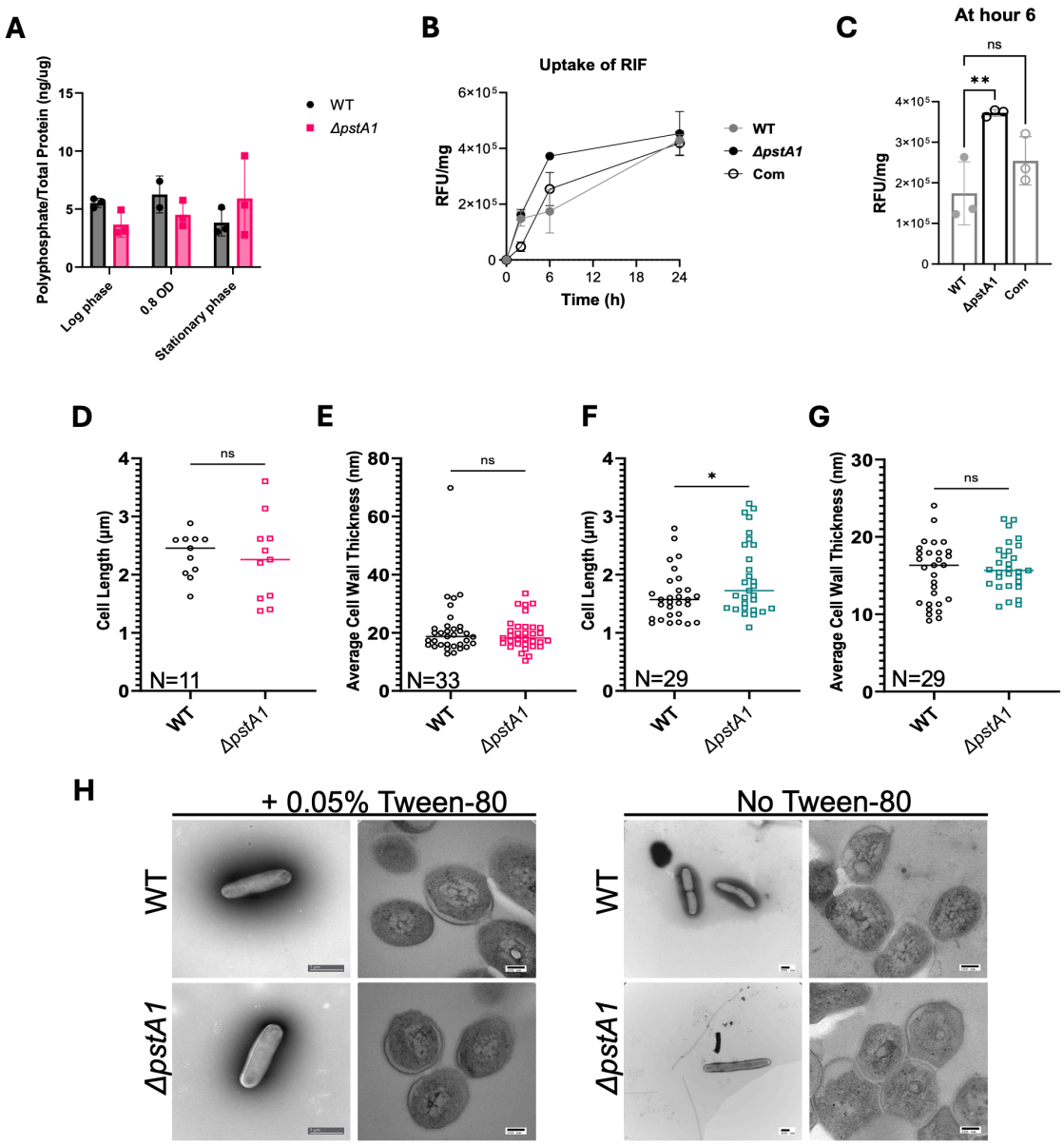

Figure 5. Rifampin uptake kinetics and cell morphology analysis of Δ*pstA1*. (**A**) Intracellular polyphosphate levels across different growth phases for wild-type and Δ*pstA1* normalized to total protein concentration. No significant differences were observed by one-way ANOVA followed by Tukey's multiple comparisons test. (**B-C**) Rifampin uptake kinetics in wild-type, Δ*pstA1*, and *pstA1* complement strains measured in a filter culture system. Bacteria were treated with 1.0 μg/mL rifampin and uptake was calculated as (initial rifampin concentration in media at 0 h - rifampin concentration at each timepoint) normalized to protein concentration. (**D-E**) Cell length and average cell

812 wall thickness of wild-type and Δ*pstA1* cultures grown in 7H9 medium with 0.05% Tween-
813 80 during log phase. (**F-G**) Cell length and average cell wall thickness of cultures grown
814 without Tween-80. Cell length measurements: n=11 bacteria per strain (with Tween-80),
815 n=29 bacteria per strain (without Tween-80). Cell wall thickness was determined by
816 averaging two measurements per bacterium: n=33 bacteria per strain (with Tween-80),
817 n=29 bacteria per strain (without Tween-80). (**H**) Representative transmission electron
818 microscopy images of whole bacteria or thin sections from log-phase cultures grown with
819 or without 0.05% Tween-80. Data represent mean ± SD. Statistical significance was
820 determined by one-way ANOVA followed by Tukey's multiple comparisons test (**B-C**) or
821 unpaired t-test (**D-G**). $^{**}P \leq 0.01$; $^{*}P \leq 0.05$; ns, not significant.

822

823

824

825

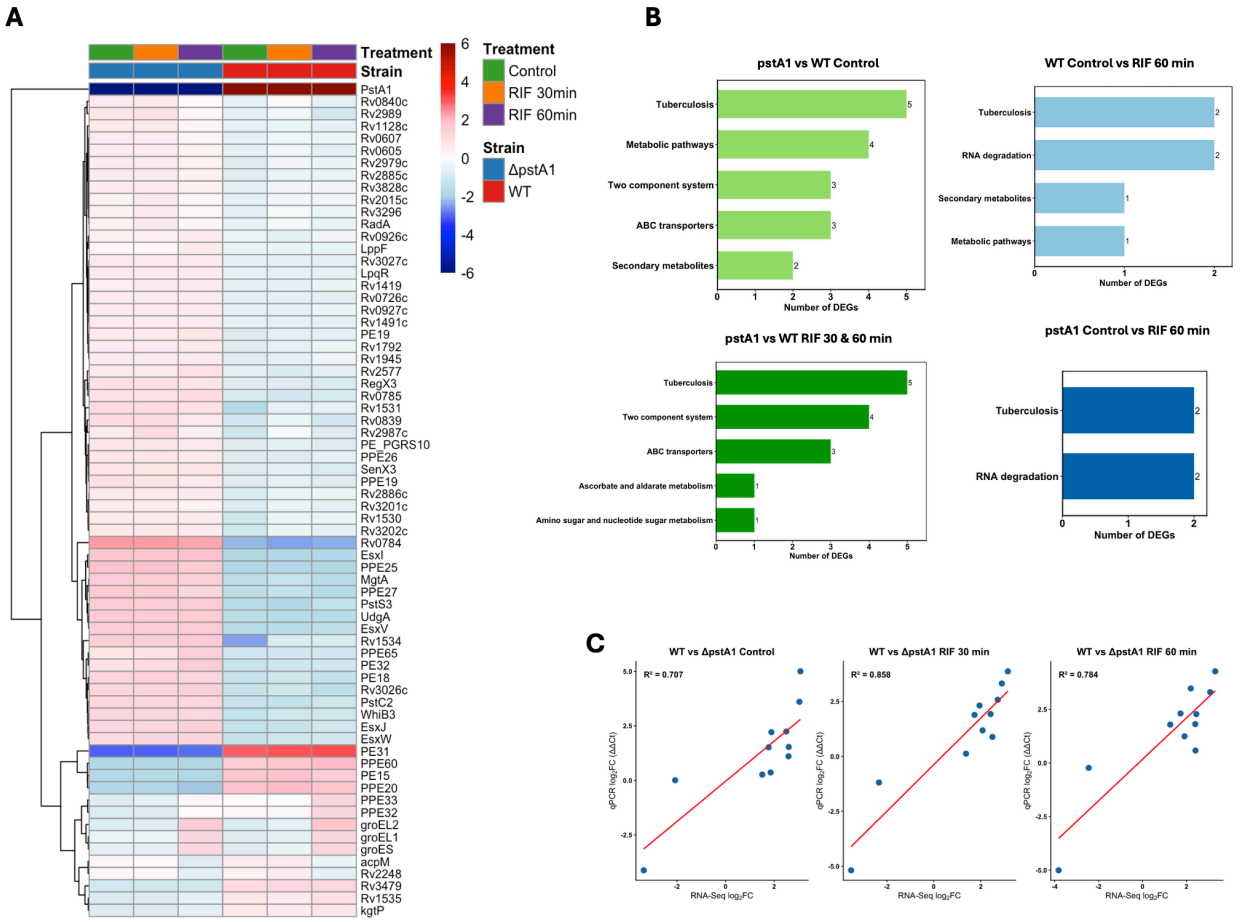

Figure 6. Transcriptional profiling of Δ*pstA1* with and without rifampin treatment. (**A**) Heatmap of differentially expressed genes (DEGs) in wild-type and Δ*pstA1* strains at baseline and after rifampin treatment (30 and 60 min). Genes were filtered for absolute $\log_2$ fold change ≥ 1 and adjusted $P < 0.05$. Each row represents a gene, and each column represents a biological replicate. Color scale indicates $\log_2$ fold change relative to wild-type control. (**B**) Functional enrichment analysis of DEGs for key comparisons: Δ*pstA1* vs wild-type control (top left), wild-type control vs wild-type with 60 min rifampin treatment (top right), Δ*pstA1* control vs Δ*pstA1* with rifampin treatment at 30 and 60 min (bottom left), and wild-type control vs Δ*pstA1* with 60 min rifampin treatment (bottom right). Bar plots show the number of DEGs in each functional category. Correlation between RNA-seq and RT-qPCR validation for selected genes across three comparisons. Each point represents a gene, with correlation coefficients (R^2) indicated for each comparison.

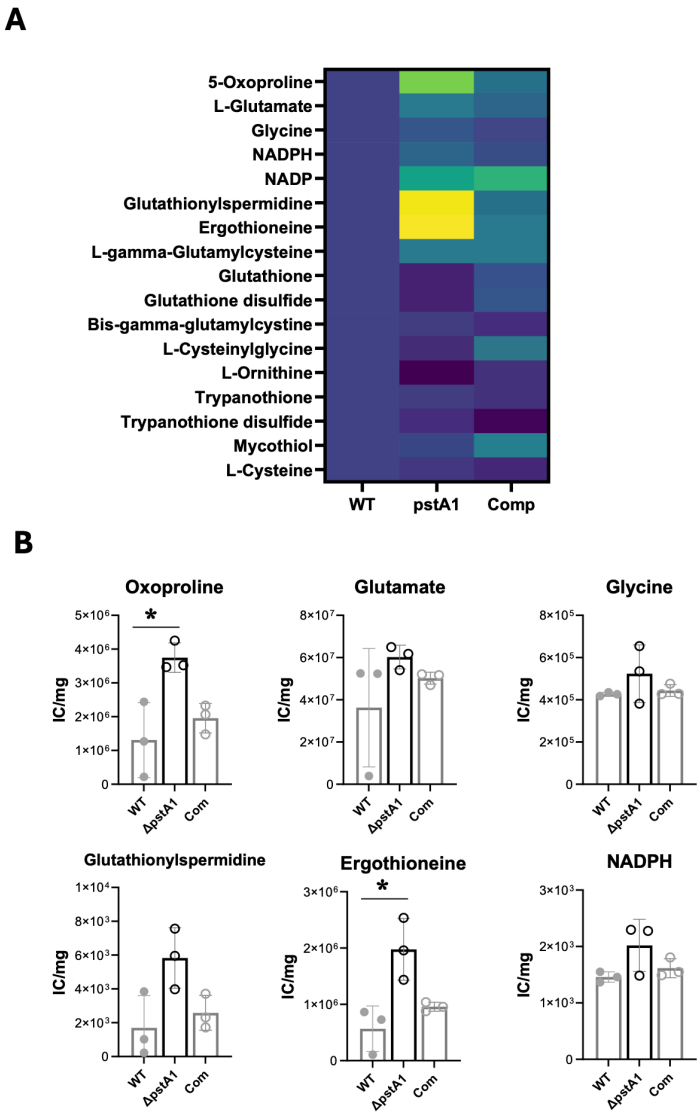

Figure 7. Metabolomic profiling reveals elevated antioxidant metabolites in rifampin-treated Δ*pstA1*. (**A**) Heatmap showing relative abundances of intracellular metabolites involved in antioxidant and redox pathways in wild type, Δ*pstA1*, and *pstA1* complement strains after 6 hours of rifampin exposure. Color scale indicates relative metabolite abundance (normalized to internal standards and protein concentration). (**B**) Quantification of selected antioxidant pathway metabolites. Bars represent mean ± SEM from three biological replicates. Statistical significance was determined by one-way ANOVA followed by Tukey's multiple comparisons test ($P < 0.1$).

Supplementary Figures

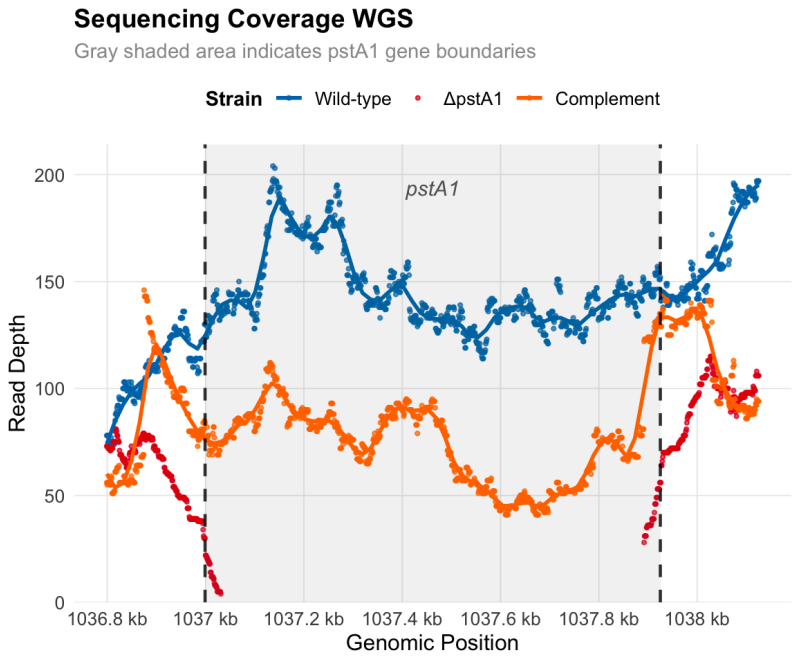

Figure S1. Whole genome sequencing of pstA1 deletion and complementation strains.

Read depth coverage across the *pstA1* locus in wild-type H37Rv (blue), ΔpstA1 deletion mutant (red), and Δ*pstA1::pstA1* complement strain (orange). Gray shaded region indicates pstA1 gene boundaries (coordinates 1,036,999-1,037,925 bp). Vertical dashed lines mark gene start and end positions. Wild-type exhibits uniform coverage (~150-200× read depth) throughout the *pstA1* coding sequence. The Δ*pstA1* strain shows near-zero coverage within the deleted region with maintained coverage in flanking sequences, confirming successful targeted deletion. The complement strain displays reduced coverage (~50-100× read depth) within *pstA1* relative to wild-type, consistent with episomal expression from the pMH94 plasmid. Individual points represent sequencing depth at each nucleotide position; smoothed trend lines (LOESS, span = 0.1) are shown for wild-type and *pstA1* complement strains. Coverage was calculated from reads aligned to the *M. tuberculosis* H37Rv reference genome using samtools depth and visualized in R.

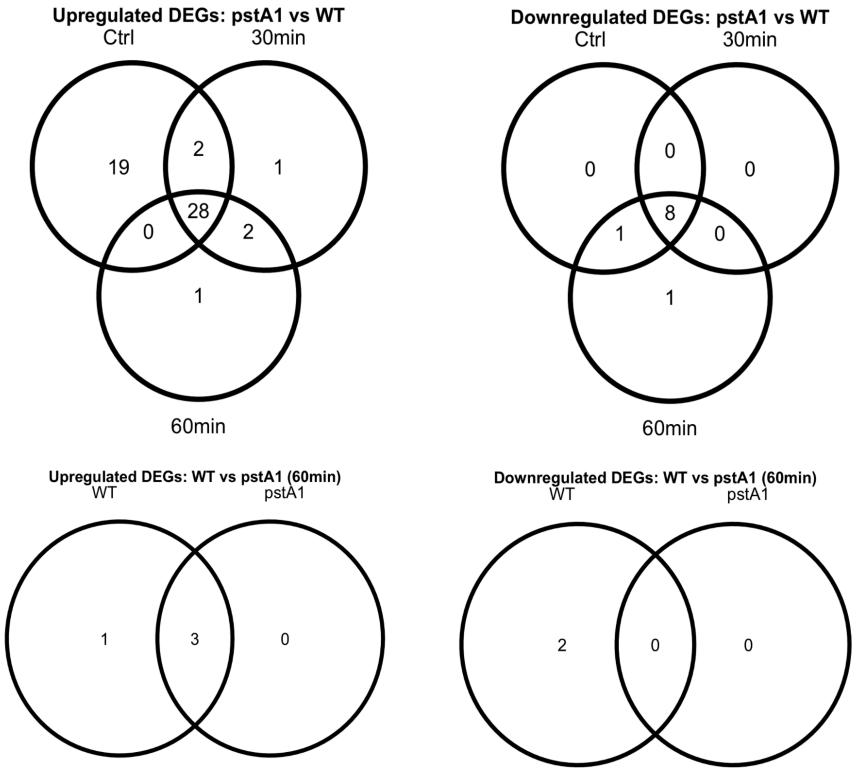

Figure S2. Venn diagram analysis of differentially expressed genes between Δ*pstA1* and wild-type strains. Overlap of differentially expressed genes (DEGs) identified by RNA-seq (log2 fold change > 1, adjusted p-value < 0.05). Top panels show upregulated (left) and downregulated (right) genes in Δ*pstA1* compared to WT across control, 30 min, and 60 min rifampin treatment conditions. Bottom panels show upregulated (left) and downregulated (right) genes comparing WT and Δ*pstA1* responses to 60 min rifampin treatment relative to their respective untreated controls. Numbers indicate the count of unique or shared DEGs in each category.

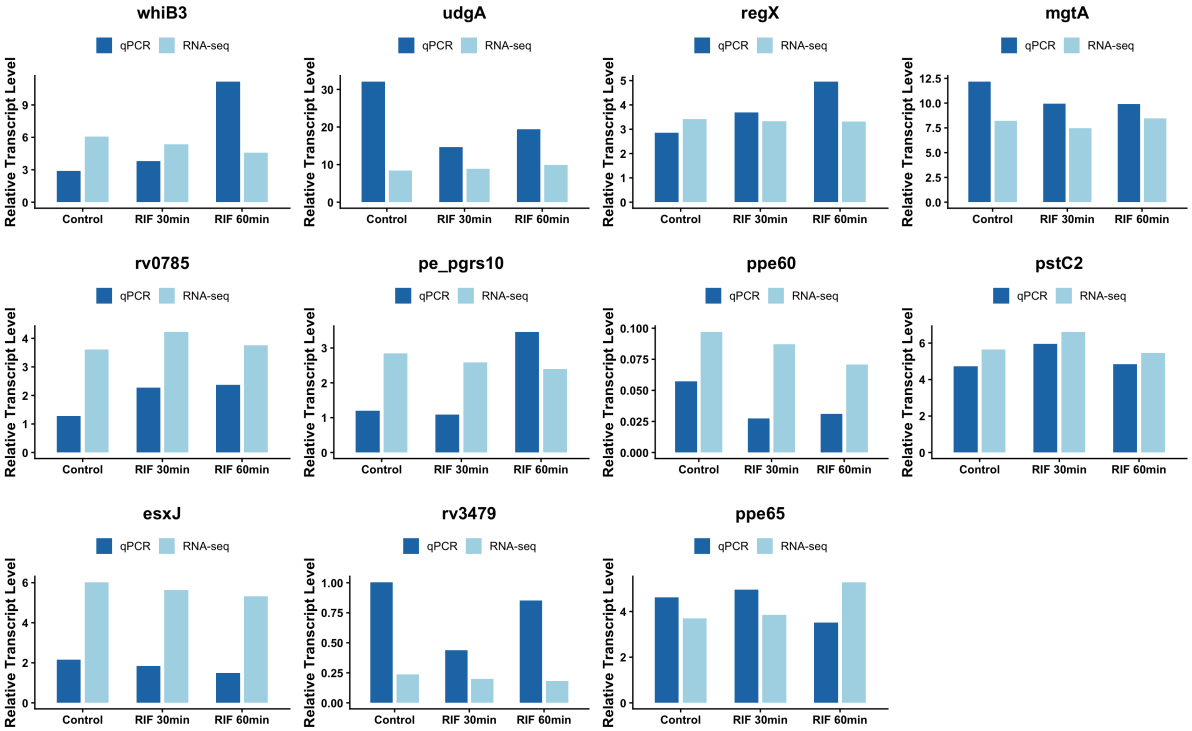

Figure S3. Validation of RNA-seq results by quantitative PCR. Comparison of transcript levels measured by RNA-seq (light blue) and qPCR (dark blue) for selected differentially expressed genes in wild-type *M. tuberculosis* under control conditions and following 30- or 60-min rifampin treatment. Genes were selected to represent diverse functional categories including transcriptional regulators (whiB3, regX), metabolic enzymes (udgA, mgtA), PE/PPE family proteins (pe_pgrs10, ppe60, ppe65, rv3479), phosphate transport (pstC2), and ESX secretion (esxJ). Relative transcript levels are normalized to control conditions. Strong correlation between RNA-seq and qPCR measurements validates the RNA-seq dataset.

896 **Supplementary Table S1. Oligonucleotide primers used for RT-qPCR analysis of**
897 ***Mycobacterium tuberculosis* genes**

Target Gene	Direction	Sequence (5′→3′)	Length (bp)	GC Content (%)	Melting Temperature (°C)	Amplicon Size (bp)
sigA	Forward	CGACGAAGACCACGAAGAC	19	57.9	62	131
sigA	Reverse	CGTCTTCATCCCAGACGAAAT	21	47.6	62	
pstA1	Forward	CGTTGGTCCTGCTGATGTT	19	52.6	62	111
pstA1	Reverse	TCCATTTCGGAACGCCTAAC	20	50.0	62	
whiB3	Forward	ACTCATCGATGTTCTTCCATCC	22	45.5	62	147
whiB3	Reverse	AAACGCCATAGGGCTCAC	18	55.6	62	
udgA	Forward	GTCCACGTGTACGATCCAAAG	21	52.4	63	123
udgA	Reverse	CCATTCGGTAAGCACCAACA	20	50.0	63	
regX	Forward	CTACGTGACCAAGCCCTATTC	21	52.4	62	132
regX	Reverse	TCCACATCCATGCGAACC	18	55.6	62	
mgtA	Forward	CACCTTCCGAATGCTGAGA	19	52.6	62	145
mgtA	Reverse	CGGAACATCGGTTTGGTAGA	20	50.0	62	
rv0785	Forward	GGCACGGTATCCGGATTATT	20	50.0	62	132
rv0785	Reverse	CATGTCCAGACTTGGTGATGTA	22	45.5	62	
pe_pgrs10	Forward	CAACACGACGGGATTGTTGA	20	50.0	63	131
pe_pgrs10	Reverse	GCACGAACTGGGCGTAAA	18	55.6	63	
ppe60	Forward	TCAGCAACGTCAGTTCGATAG	21	47.6	62	100
ppe60	Reverse	GGAGCTAAGCCCTTCAACAT	20	50.0	62	
pstC2	Forward	GGCGAATCACGCCAATTTC	19	52.6	62	117
pstC2	Reverse	AGAGCCGTTATCGAACTCAAC	21	47.6	62	
esxJ	Forward	GACACCATGACCCAGATGAAT	21	47.6	62	108
esxJ	Reverse	CTGCTCTTGCTGTTCGTAGT	20	50.0	62	
rv3479	Forward	TCCGATCTCAGTGTGCTAGT	20	50.0	62	112
rv3479	Reverse	CCGTGGATTGTTGGAGATAGTC	22	50.0	62	
ppe65	Forward	GCAGTTGTCGCCATTCAATC	20	50.0	62	144
ppe65	Reverse	CTAAGCCCAAACAACGCTTTAG	22	45.5	62	

898 **Abbreviations:** bp, base pairs; GC, guanine-cytosine; RT-qPCR, reverse transcription
899 quantitative polymerase chain reaction.

All primers were designed to amplify *Mycobacterium tuberculosis* target genes. Primer pairs generate amplicons ranging from 100 to 147 bp in length.

Supplementary Table S2. All genes meeting the significance threshold (|log2 fold change| > 1, adjusted p-value < 0.05) across seven pairwise comparisons are listed. Comparisons include temporal responses to rifampin treatment in wild-type and Δ*pstA1* strains (30 and 60 min versus untreated controls), and strain-specific differences between Δ*pstA1* and wild-type under control and rifampin-treated conditions. For each gene, the following information is provided: comparison name, *M. tuberculosis* H37Rv gene identifier (Rv number), gene name, log2 fold change, adjusted p-value (Benjamini-Hochberg correction), and KEGG pathway annotations where available. A total of 58 genes were differentially expressed between Δ*pstA1* and wild-type under control conditions (49 upregulated, 9 downregulated), 41 at 30 min rifampin (33 upregulated, 8 downregulated), and 41 at 60 min rifampin (31 upregulated, 10 downregulated). Only 6 genes responded to rifampin in wild-type (4 upregulated, 2 downregulated at 60 min), and 3 genes in Δ*pstA1* (all upregulated at 60 min), highlighting the substantial transcriptional differences between the strains.